scientific reports

OPEN

Thermal excitation signals in the inhomogeneous warm dense electron gas

Zhandos A. Moldabekov[1,2], Tobias Dornheim[1,2] & Attila Cangi[1,2]✉

We investigate the emergence of electronic excitations from the inhomogeneous electronic structure at warm dense matter parameters based on first-principles calculations. The emerging modes are controlled by the imposed perturbation amplitude. They include satellite signals around the standard plasmon feature, transformation of plasmons to optical modes, and double-plasmon modes. These modes exhibit a pronounced dependence on the temperature. This makes them potentially invaluable for the diagnostics of plasma parameters in the warm dense matter regime. We demonstrate that these modes can be probed with present experimental techniques.

An emerging research area where electronic excitations—such as plasmons[1]—play a central role is warm dense matter (WDM)[2–4]. Research on WDM has received increased attention due to its relevance for fusion energy experiments, novel materials discovery, and high-energy astrophysical phenomena. From a technological point of view, warm dense conditions occur in the heating process of inertial confinement fusion capsules[5,6]. In terms of materials science, understanding WDM propels the discovery of unexplored material properties such as novel chemistry[7,8], non-equilibrium effects[9,10], and phase transitions[11]. On a fundamental science level, probing warm dense conditions is essential for obtaining new insights on astrophysical objects, such as Earth's core[12,13], the interior of both solar planets[14–16] and exoplanets[17,18], the properties of brown and white dwarfs[19,20], and neutron stars[21].

One labels the state of matter as WDM when (1) the Fermi energy E_F and characteristic thermal energy of electrons $k_B T$ have the same order of magnitude, i.e., $\theta = k_B T/E_F \sim 1$ and (2) electrons are strongly correlated, i.e., $r_s = a/a_B \geq 1$ where a denotes mean interelectronic distance and a_B the first Bohr radius[22]. Additionally, WDM phenomena are transient in experiments—covering the range from femtoseconds to picoseconds. Studying WDM phenomena is therefore highly challenging[2,23]—common concepts from well-established fields of physics do not apply: the persistence of quantum effects and strong coupling renders plasma physics concepts inaccurate, while accurate approaches from condensed-matter physics are often infeasible due to the length, time, and temperature scales involved.

The aforementioned applications and the intricate nature of WDM have triggered a growing number of cutting-edge experimental activities, often in large-scale research facilities[24–29]. The array of experimental techniques that probe excitations in WDM include X-Ray absorption spectroscopy[30], emission spectroscopy[31,32], X-Ray Thomson scattering[33], resonant inelastic X-Ray scattering[34], and the most recently developed ultrafast multi-cycle terahertz measurement technique[35].

Due to its challenging nature, reliable diagnostics of WDM properties (such as temperature and density) can only be achieved by joint efforts of experimental campaigns with accurate, first-principles modeling techniques[36,37]. For example, consider determining the electronic temperature in warm dense samples. In principle, the temperature can be obtained from the detailed balance of the dynamic structure factor[38] that is probed in X-Ray Thomson scattering. In practice, however, the noise in the measured signals renders a purely experimental temperature determination inaccurate[39].

Historically, WDM modeling has relied on dielectric models such as the random-phase approximation[40], and a formally exact formulation of dielectric models is provided by the local field correction[41]. Their accurate parametrization is provided by quantum Monte-Carlo calculations of the uniform electron gas in its ground state[42,43] and at finite temperature[44,45]. A notable example is the recently introduced effective static approximation[46,47]. Extensions of dielectric models to take into account electron-ion collisions are based on the Mermin approach (MA)[48–50], but only in an approximate manner. An alternative simulation method for WDM diagnostics is Kohn-Sham density functional theory (KS-DFT)[51,52] and its extension to the time domain[53]. Similar to dielectric models, the electron-electron correlation is approximated in practice, but electron-ion collisions are tackled more

[1]Center for Advanced Systems Understanding (CASUS), 02826 Görlitz, Germany. [2]Helmholtz-Zentrum Dresden-Rossendorf (HZDR), 01328 Dresden, Germany. ✉email: a.cangi@hzdr.de

directly. These calculations have become the workhorse among modern simulation methods in materials[54,55] and most recently also for WDM modeling[56–58].

In prior diagnostics efforts of WDM, a homogeneous electronic structure of the samples has commonly been assumed, particularly regarding the modeling aspects. Under this assumption, the electronic temperature of the induced WDM states has been determined from X-Ray Thomson scattering signals, for instance, in warm dense aluminum either by dielectric models[59] or KS-DFT calculations[57,58,60]. Despite the combined efforts of experiment and simulation, determining the electronic temperature is still subject to significant uncertainties[61]. Assuming a homogeneous WDM sample is justified when relaxation effects are considered. Their time scale is typically on the order of several picoseconds[22,62]. Moreover, this assumption underpins the uniform electron gas[42,45] as a paradigm for modeling phenomena in WDM.

In this Report, we break away from the common assumption of a homogeneous electronic structure in WDM diagnostics. We (1) show the emergence of yet unexplored modes of electronic excitations in *inhomogeneous* WDM, (2) illustrate the potential utility of these modes for the temperature diagnostics of WDM, and (3) numerically demonstrate the emergence of these modes in the inhomogeneous electronic structure imposed on warm dense aluminum.

We show that features in the new modes are absent in the spectrum of homogeneous WDM states which is dominated by the well-known plasmon mode. The variety of features we observe depends on the degree of the density deviation from the homogeneous state. They include satellite signals around the standard plasmon feature, transformation of plasmons to optical modes, and double-plasmon modes. We demonstrate that both the realization of the required perturbation amplitudes and the observation of the proposed features are feasible using present and upcoming experimental facilities[25,63–66]. For example, the dynamics of emerging electronic structures was recently shown in laser-driven WDM samples where inhomogeneities were imposed by a periodic grating structure[65]. Furthermore, spatially modulating electronic structures can also be triggered by free electron[25], VUV[67], and THz lasers[66]. Therefore, we discuss the temperature dependence of excitation signals in the inhomogeneous warm dense electron gas that can be utilized for WDM diagnostics.

Results

Our investigation begins with imposing spatial modulations on the warm dense uniform electron gas (UEG) in terms of the Hamiltonian

$$H = H_{\mathrm{UEG}} + \sum_{i=1}^{N} 2U_0 \cos\left(\boldsymbol{r}_i \cdot \mathbf{Q}\right), \tag{1}$$

where N is the total number of electrons and H_{UEG} the standard Hamiltonian of the interacting UEG. Note that we adopt Hartree atomic units, where the length is expressed in Bohr and the energy in Hartree. This elementary Hamiltonian captures the fundamental physics that leads to the proposed modes. Likewise, it is motivated by the fact that electronic oscillations in WDM are well described by the UEG due to the relatively weak electron-ion coupling[46,68,69]. In Eq. (1), the degree of inhomogeneity is determined by the perturbation amplitude U_0. The length scale of the imposed modulations is set by the wave vector $\mathbf{Q}$. This Hamiltonian has been used extensively in prior work to study response properties of ambient and warm dense electrons with respect to local field corrections[43,70] and response functions[71,72].

We utilize the electron energy-loss function (EELF) to illustrate the emergence of electronic excitations in inhomogeneous WDM

$$\mathscr{L}(\mathbf{q}, \omega) = -\mathrm{Im}\left[\frac{1}{\varepsilon(\mathbf{q}, \omega)}\right], \tag{2}$$

which is defined in terms of the macroscopic dielectric function $\varepsilon(\mathbf{q}, \omega)$[73]. Electronic excitations are identified by distinct features located at the maxima of the EELF[74].

The EELF is proportional to the double-differential cross section in inelastic electron scattering. It is measured directly in electron energy-loss spectroscopy[75]. Likewise, the X-Ray Thomson scattering signal is proportional to the EELF via the dynamical structure factor[36] obtained from the fluctuation-dissipation theorem[76]. The electronic excitations we predict are computed using first-principles calculations of the EELF based on the Hamiltonian in Eq. (1). We use time-dependent KS-DFT[53] as implemented in the GPAW code[77–80] and employ the adiabatic local density approximation[81]. We corroborate the accuracy of our results based on the electronic density of the initial state associated with Eq. (1). For this purpose, we compare our KS-DFT calculations with quantum Monte-Carlo calculations. This comparison is meaningful, as the KS states that comprise the total electronic density are used to compute the EELF of the perturbed system. We provide all computational details in the "Methods" section. Furthermore, we also rule out a source of systematic errors by providing an extensive analysis of finite size effects[82].

In the following, we consider the typical range of WDM conditions[3] with a density parameter $r_s = 2$ (corresponding to an electron number density $n \simeq 2 \times 10^{23} \ \mathrm{cm}^{-3}$) and a degeneracy parameter θ in the range from 0.1 to 1.0.

The choice of amplitude and wave number of the perturbation is grounded in our interest of inhomogeneities on excitations which become relevant when $q/q_F \ll 1$[83]. We therefore consider U_0 in the range from 0.1 to 1.0 and $Q \simeq 0.84q_F = 1.5 \ \text{Å}^{-1}$. Furthermore, these perturbation parameters are viable in current experimental setups[65,72]. For example, available THz lasers with an intensity of 600 kV/cm[66] correspond to a perturbation amplitude $U_0 \simeq 0.3$[72]. Likewise, free electron lasers with intensities of up to $10^{22} \ \mathrm{W/cm}^2$[25] provide perturbation
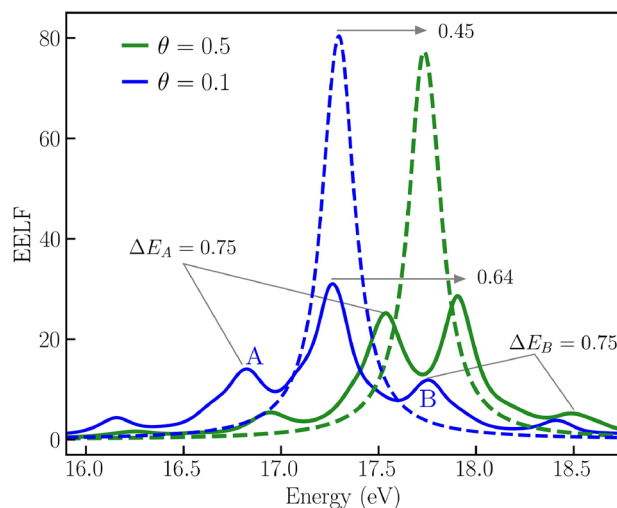
Figure 1. A novel mode of electronic excitation (solid blue and green curves) that emerges in inhomogeneous WDM. The new mode is observed in the EELF along the wave vector. **Q** when a perturbation amplitude $U_0 = 0.1$ is imposed on the electronic structure. The EELF is shown for $q = 0.431$ Å^{-1} at temperatures $\theta = 0.5$ (solid blue) and $\theta = 0.1$ (solid green). The new mode differs significantly from the well-explored plasmon mode (dashed blue and green curves). It also has a pronounced temperature dependence.

amplitudes up to $U_0 \approx 2$. Alternatively, periodically inhomogeneous electronic structures can be generated using laser irradiation of pre-designed grating targets[65].

Our central result is illustrated in Fig. 1. It displays a new mode of electronic excitation (solid blue and solid green) that emerges in inhomogeneous WDM due to the perturbation in Eq. (1). Additionally, the figure displays the pronounced temperature dependence of the new mode (solid blue versus solid green). We highlight the generality of these new modes by deliberately focusing on the interacting electron gas. Furthermore, we also demonstrate the emergence of these modes in isochorically heated Aluminum towards the end.

In Fig. 1, the EELF is shown for **q** $= 0.431$ Å^{-1}. The predicted mode emerges in the direction along the wave vector **Q**. It is shown at two temperatures corresponding to $\theta = 0.5$ (solid blue) and $\theta = 0.1$ (solid green). It exhibits a rich structure distinctly different from the well-known plasmon mode (dashed blue and dashed green). The new mode exhibits a damped structure close to the position of the plasmon peak and shows several satellite peaks. More importantly, the new mode has a strong temperature dependence. The broadened feature in the new mode is shifted by about 0.64 eV when the temperature is increased, while the plasmon mode is shifted by about 0.45 eV. The shift in the satellite peaks (A and B) is stronger, roughly $\Delta E_A \approx 0.75$ eV and $\Delta E_B \approx 0.75$ eV. Besides their energy shift, we expect the emergence of satellite peaks to be potentially helpful for diagnostics.

Next in Fig. 2, we predict additional modes and features that are observed along the wave vector **Q** for various values of **q**. These features emerge when we assess a wider range of perturbation amplitudes. We consider both a weak perturbation amplitude $U_0 = 0.1$ and a strong amplitude $U_0 = 1.0$. We simultaneously probe the temperature dependence of these new modes for increasing values of the degeneracy parameter, $\theta = 0.1$ (temperature $T \simeq 1.25$ eV, solid blue), $\theta = 0.5$ ($T \simeq 6.27$ eV, solid green), and $\theta = 1.0$ ($T \simeq 12.54$ eV, solid red).

First (left panel of Fig. 2), we assess the emerging mode when the perturbation is weak ($U_0 = 0.1$). At low temperature ($\theta = 0.1$), the mode remains centered around the same frequency, but its satellite features become more separated with increasing **q**. With increasing temperature the mode peak intensity also rises and shifts to higher energies. Conversely, the satellite peaks become increasingly suppressed. This is due to thermal excitations that decrease the effect of the inhomogeneity.

Next in the right panel of Fig. 2, we further increase the perturbation amplitude (to $U_0 = 1.0$). This leads to a transformation of the plasmon mode to an *optical mode*. The physics behind this transformation is a localization effect. Due to the strong perturbation, a large number of electrons becomes localized in the strong density enhancement regions. This is a manifestation of electron density oscillations around the center of mass of these localized regions. We observe that the energy of the *optical mode* strongly depends on temperature. For example, at the smallest considered wave number $q = 0.048$ Å, the energy of the *optical mode* shifts by 0.4 eV from 32 eV at $\theta = 0.1$ to 31.6 eV at $\theta = 0.5$. A further increase of the degeneracy parameter to $\theta = 1.0$ results in a significant shift of the *optical mode* to $\lesssim 31$ eV.

Furthermore, we provide further supporting evidence on the observation of the modes and features predicted in Fig. 2. To that end, we provide a detailed analysis of the underlying electronic structure in Fig. 3. There, we display the density distribution of orbital densities $n_i(\mathbf{r}) = |\phi_i(\mathbf{r})|^2$ (solid grey) and the total density distribution $n(\mathbf{r}) = \sum_i f_i |\phi_i(\mathbf{r})|^2$ (solid black) along **Q** at $\theta = 1.0$, where f_i denotes the occupation numbers, here a Fermi-Dirac distribution. The left panel shows the results for a weak ($U_0 = 0.1$), the right panel for a strong ($U_0 = 1.0$) perturbation amplitude. While the KS orbitals $\phi_i(\mathbf{r})$ are, strictly speaking, auxiliary quantities, they can nevertheless be used to explain the observed behavior of the EELF qualitatively. Furthermore, we confirm the accuracy of our KS-DFT calculations by comparing them to accurate quantum Monte-Carlo calculations
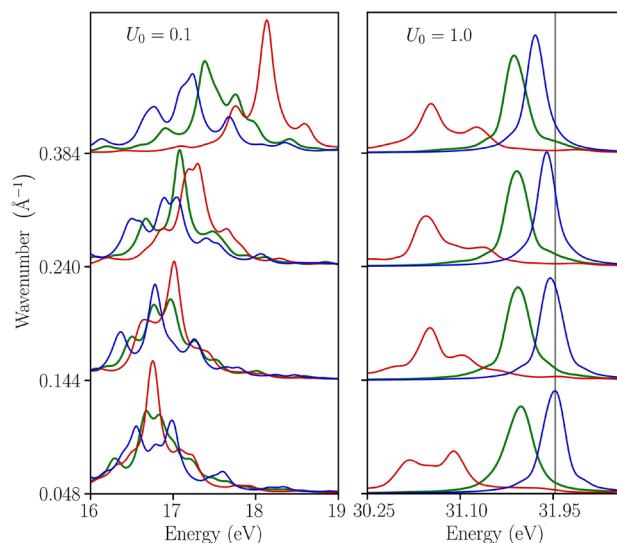
Figure 2. Novel modes in the EELF at weak and strong perturbation amplitudes. An optical mode emerges at a strong perturbation amplitude $U_0 = 1.0$. The dependence of these modes on q and on the degeneracy parameter θ (solid blue denotes $\theta = 0.1$, solid green $\theta = 0.5$, and solid red $\theta = 1.0$) is strong and depends on the imposed perturbation amplitude U_0. The vertical grey line is a guide to the eye and helps to observe that at $U_0 = 1.0$ the dispersion shifts to lower frequencies with increasing wave vector q.
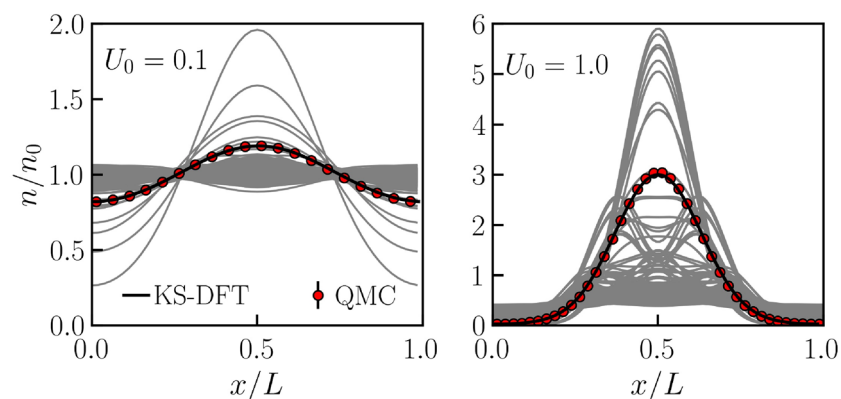
Figure 3. Analysis of the electronic structure for a weak ($U_0 = 0.1$) and strong ($U_0 = 1.0$) perturbation amplitude at a degeneracy parameter $\theta = 1.0$. The orbital density (solid grey) and the total density (solid black) distributions from KS-DFT calculations provide an explanation for the emergence of the collective modes and features illustrated in Fig. 2. For illustrative purposes, the orbital density is scaled by the number of electrons. Furthermore, the comparison with quantum Monte-Carlo calculations (red circles) demonstrates the accuracy of our KS-DFT results.

based on the Hamiltonian in Eq. (1). As shown, the total density distribution from KS-DFT (solid black) agrees very well with the quantum Monte-Carlo results (red circles) throughout.

At $U_0 = 0.1$, most of the orbitals are spread across the simulation domain and several orbitals show a significant deviation from uniformity. This leads to the formation of satellite peaks around the plasmon peak observed in the left panel of Fig. 3. At $U_0 = 1.0$, most of the orbitals are localized at the central region. This causes the formation of an optical mode due to the collective oscillation of these orbitals around the center of the localization region. Further increase in U_0 leads to a stronger signal from optical modes.

So far, we discussed emerging modes along the direction of **Q**. However, in the transpose direction to **Q**, the EELF of the inhomogeneous system exhibits a mode similar to the standard plasmon[82]. Next, in Fig. 4, we demonstrate the formation of a double-plasmon mode at an angle of 45° to **Q**. The EELF is plotted for a perturbation amplitude of $U_0 = 1.0$ at various temperatures. The double plasmon signal appears at well separated energies. For example, at $q = 0.136$ Å one signal emerges around 10.7 eV and the other in the range from 29.1 eV to 30.1 eV. The plasmon excitation at larger energies is particularly sensitive to thermal effects. It shifts by about 0.9 eV when θ increases from 0.1 to 1.0.
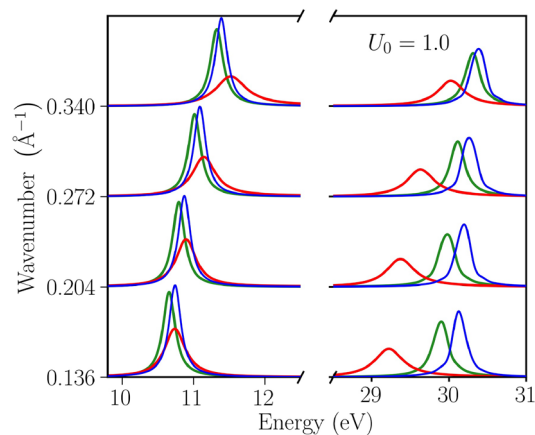
Figure 4. The emergence of a double-plasmon mode is observed at an angle of 45° to **Q**. The EELF is shown at a perturbation amplitude $U_0 = 1.0$ and for increasing temperature where solid blue denotes $\theta = 0.1$, solid green $\theta = 0.5$, and solid red $\theta = 1.0$. The double-plasmon feature exhibits a pronounced dependence on the temperature.
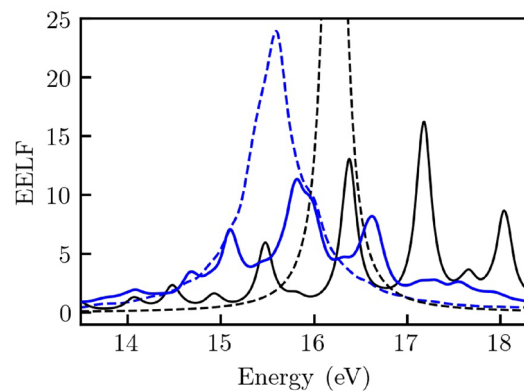

Figure 5. The emergence of novel modes of electronic excitations in isochorically heated aluminum. The EELF for aluminum at $U_0 = 0.1$, $T = 1.25$ eV along wave vector **Q** in the presence of externally imposed inhomogeneity (solid blue) and in the absence of the perturbation (dashed blue) at ($q = 0.34$ Å^{-1}). The results for the uniform (solid black) and perturbed electron gas (dashed black) at $q = 0.37$ Å^{-1} are shown for comparison.

We conclude this Report by demonstrating the emergence of these novel modes in isochorically heated aluminum. To this end, we impose an inhomogeneous electronic structure by applying the same perturbation as in Eq. (1). The final results of our analysis are shown in Figs. 5 and 6. Figure 5 illustrates the EELF in aluminum without any perturbation (dashed blue) and when the perturbation in Eq. (1) is imposed (solid blue). This is compared against the uniform (dashed black) and perturbed electron gas (solid black) as defined in Eq. (1). In Fig. 6, we illustrate the temperature dependence of the predicted features in aluminum. The peak of the feature in aluminum shifts by about 0.4 eV when the temperature increases from 1.25 eV (solid blue) to 6.27 eV (solid green). The results for an unperturbed electronic structure in aluminum are provided as a reference (dashed blue and green). The comparison between solid and dashed curves further illustrates the effect a perturbed electronic structure has—while the peak position in the unperturbed case (dashed blue vs. dashed green curves) does not change significantly with temperature, a clear shift is observed in the perturbed case (solid blue vs. solid green curves).

Experimental feasibility

We demonstrate that the resolution achieved in present experiments is sufficient to measure the predicted electronic excitations that emerge in inhomogeneous WDM. To that end, in Fig. 7 we show the EELF at the wave-number at which the plasmon signal was detected in a recent experiment on Aluminum[84]. We observe that, first of all, our calculations in the homogeneous system reproduce the plasmon position (black curve) measured in the experiment (purple data point). Secondly, our predicted features in inhomogeneous WDM (blue curve) can be resolved with the current experimental accuracy, i.e., the uncertainty in the experimentally measured plasmon energy (dashed purple) is sufficiently small. Importantly, this example is as an illustration and,
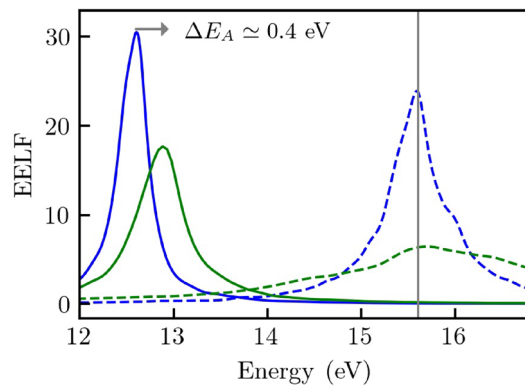
Figure 6. The EELF for aluminum at $U_0 = 0.5$, $q = 0.34$ Å^{-1} at temperatures $T = 1.25$ eV (solid blue) and $T = 6.27$ eV (solid green). The EELF of the unperturbed aluminum (dashed) is shown for comparison.
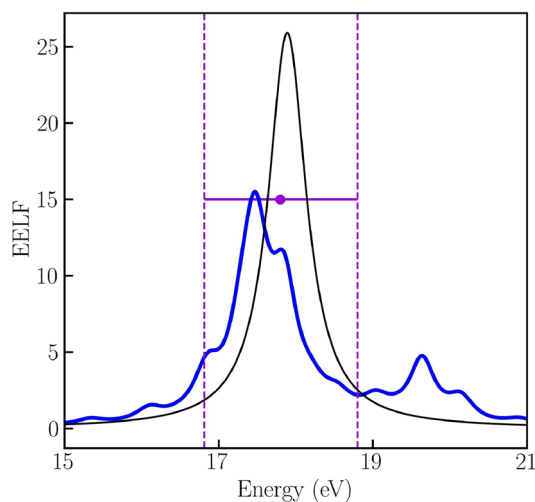

Figure 7. The EELF at $U_0 = 0.1$, $\theta = 0.024$, $q = 0.62$ Å^{-1}. Circle symbol indicates position of the experimentally measured plasmon location of the homogeneous WDM[84]. Vertical dashed curves correspond to uncertainty range in the experiment. The solid black curve illustrates the plasmon mode, i.e., the EELF of the uniform electron gas. The EELF of the inhomogeneous state (along wave vector **Q**) is illustrated as the solid blue curve.

in general, other (smaller) values of the wave numbers can be probed. We note that recently an energy resolution better than 0.1 eV for diagnostics using inelastic X-ray scattering at the high energy density instrument of the European XFEL has been reported[85]. This enables probing various new features in the electronic excitation spectrum discussed in this work.

Conclusion

We have demonstrated the emergence of novel electronic excitations in the inhomogeneous warm dense electron gas. From a physical perspective, the well-known plasmon is transformed into a more complicated mode with multiple peaks. Its details can be readily controlled via the imposed perturbation amplitude. Ultimately, an increasing degree of inhomogeneity results in both an optical mode and a double-plasmon feature. These physical effects are interesting in their own right, and the required perturbation amplitudes can be realized in experimental facilities. We also show that the energy resolution of present experiments[85] is sufficient to resolve the emerging modes and features.

From a practical point of view, the presented EELF spectra of inhomogeneous WDM exhibit a substantially stronger dependence on the electronic temperature than the standard plasmon in homogeneous WDM. Furthermore, their directional dependence and richer structure provide additional constraints on theory and simulation. This can be used to solve the long-standing problem of temperature diagnostics in WDM, which is rather unconstrained at present.

The inhomogeneous electron structures that we investigate in this work can be realized using various already existing experimental setups. For example, sufficient perturbation amplitudes (see Ref.[72] for details) can be realized at LCLS[25], the European X-FEL[28], and FLASH[86]. A particularly promising experimental setup capable of

measuring dynamics following intense terahertz excitation of 600 kV/cm[66] (corresponding to a perturbation amplitude $U_0 \simeq 0.3$) has been developed at SLAC. This setup combines a picosecond terahertz pulse with an electron beam diagnostics operating on the femtosecond time scale. Finally, it is also a viable option to impose an inhomogeneity in the electronic structure by target design. Grating structures[87] can be used to fabricate targets with a spatial modulation that will impose an inhomogeneity in the electronic structure. Here, the required perturbation amplitude can be controlled in the manufacturing of the target.

While the presented results assume a harmonic perturbation, we expect that other forms of electronic perturbations—characterized by amplitudes and wave numbers comparable to those considered here, will lead to similar results. In particular, these will lead to deviations in the electronic excitation spectrum from what is expected in the unperturbed case. Therefore, we speculate that other forms of density perturbations, if realizable in experiments, can also be used for improved WDM diagnostics.

We expect that the interplay of experiment and simulation in probing inhomogeneous WDM will potentially become an invaluable new method of diagnostics enabling the reliable inference of important plasma parameters. Prospective work to confirm our predictions in WDM experiments is planned.

Methods

The time-dependent density functional theory (TDDFT) calculations were performed with the GPAW code[77–80]. We used the Perdew-Zunger LDA functional[81] in the adiabatic approximation, periodic boundary conditions, and 14 unpolarized electrons in the simulation cell. The results are computed using 40 bands at $\theta = 0.1$, 95 bands at $\theta = 0.5$, and 180 bands at $\theta = 1.0$. The momentum transfer parameter q of the EELF spectrum is restricted to the difference between two k points from the equilibrium state calculation. In the longitudinal and transverse directions with respect to **Q**, the results where computed using 32 k-points along **q** and 8 k-points in the other directions. For example, for computing the EELF spectrum along **Q** (with **Q** chosen along the x axis), $32 \times 8 \times 8$ k-points were used.

In the case of isochorically heated Aluminum, we compute changes in the electronic structure due to both the imposed external perturbation and the electron-ion interaction. Here, the face-centered-cubic crystal structure with a lattice constant $a = 4.025$ Å was used. Correspondingly, the perturbation wave number was set to $4\pi/a$. The results where obtained using 32 k-points along **q** and 8 k-points in the other directions. The plane-wave mode was used with a cutoff energy 600 eV. We used the Perdew-Zunger LDA functional[81]. The number of bands was set to 60 at 1.25 eV and was set to 95 at 6.27 eV. Not that at 1.25 eV, the number of partially occupied states is 6. At 6.27 eV, the number of partially occupied states is 35. Remaining 54 (at 1.25 eV) and 60 (at 6.27 eV) unoccupied bands provide converged and accurate results for the EELF at considered wave numbers.

The QMC data shown in Fig. 3 have been obtained via the direct path integral Monte Carlo (PIMC) method (see, e.g., Refs.[88–90] for details) without any nodal restrictions. Furthermore, we employ the primitive factorization of the density matrix using $P = 200$ imaginary-time slices. The convergence has been checked carefully. Therefore, the PIMC reference data are exact within the given error bars and constitute an unassailable benchmark for the KS-DFT results. An analysis of finite-size effects is provided as Supplementary Information[82].

References

1. Bohm, D. & Pines, D. A collective description of electron interactions: III. Coulomb interactions in a degenerate electron gas. *Phys. Rev.* **92**, 609–625. https://doi.org/10.1103/PhysRev.92.609 (1953).
2. Graziani, F., Desjarlais, M. P., Redmer, R. & Trickey, S. B. *Frontiers and Challenges in Warm Dense Matter* (Springer, 2014).
3. Fortov, V. E. *Extreme States of Matter. High Energy Density Physics* 2nd edn. (Springer, 2016).
4. Skiff, F. & Wurtele, J. *Plasma: At the frontier of science discovery*. Technical Report, U.S. Department of Energy, Office of Sciences. Report of the panel on Frontiers of Plasma Science (2017).
5. Kritcher, A. L. *et al.* In-flight measurements of capsule shell adiabats in laser-driven implosions. *Phys. Rev. Lett.* **107**, 015002. https://doi.org/10.1103/PhysRevLett.107.015002 (2011).
6. Betti, R. & Hurricane, O. A. Inertial-confinement fusion with lasers. *Nat. Phys.* **12**, 435–448. https://doi.org/10.1038/nphys3736 (2016).
7. Tamblyn, I., Raty, J.-Y. & Bonev, S. A. Tetrahedral clustering in molten lithium under pressure. *Phys. Rev. Lett.* **101**, 075703. https://doi.org/10.1103/PhysRevLett.101.075703 (2008).
8. Brongersma, M. L., Halas, N. J & Nordlander, P. Plasmon-induced hot carrier science and technology. *Nat. Nanotechnol.* **10**, 25–34. https://doi.org/10.1038/nnano.2014.311 (2015).
9. Ping, Y. *et al.* Broadband dielectric function of nonequilibrium warm dense gold. *Phys. Rev. Lett.* **96**, 255003. https://doi.org/10.1103/PhysRevLett.96.255003 (2006).
10. Ernstorfer, R. *et al.* The formation of warm dense matter: Experimental evidence for electronic bond hardening in gold. *Science* **323**, 1033–1037. https://doi.org/10.1126/science.1162697 (2009).
11. Kandyla, M., Shih, T. & Mazur, E. Femtosecond dynamics of the laser-induced solid-to-liquid phase transition in aluminum. *Phys. Rev. B* **75**, 214107. https://doi.org/10.1103/PhysRevB.75.214107 (2007).
12. Alfè, D., Gillan, M. J. & Price, G. D. The melting curve of iron at the pressures of the Earth's core from ab initio calculations. *Nature* **401**, 462–464 (1999).
13. Nguyen, J. H. & Holmes, N. C. Melting of iron at the physical conditions of the Earth's core. *Nature* **427**, 339–342. https://doi.org/10.1038/nature02248 (2004).
14. Militzer, B., Hubbard, W. B., Vorberger, J., Tamblyn, I. & Bonev, S. A. A massive core in Jupiter predicted from first-principles simulations. *Astrophys. J.* **688**, L45–L48. https://doi.org/10.1086/594364 (2008).
15. Knudson, M. D. *et al.* Direct observation of an abrupt insulator-to-metal transition in dense liquid deuterium. *Science* **348**, 1455–1460. https://doi.org/10.1126/science.aaa7471 (2015).
16. Schöttler, M. & Redmer, R. Ab initio calculation of the miscibility diagram for hydrogen–helium mixtures. *Phys. Rev. Lett* **120**, 115703 (2018).

17. Nettelmann, N., Fortney, J. J., Kramm, U. & Redmer, R. Thermal evolution and structure models of the transiting super-Earth GJ 1214B. *Astrophys. J.* **733**, 2 (2011).
18. Kramm, U., Nettelmann, N., Fortney, J. J., Neuhäuser, R. & Redmer, R. Constraining the interior of extrasolar giant planets with the tidal Love number k_2 using the example of HAT-P-13b. *A& A* **538**, 8. https://doi.org/10.1051/0004-6361/201118141 (2012).
19. Chabrier, G., Brassard, P., Fontaine, G. & Saumon, D. Cooling sequences and color-magnitude diagrams for cool white dwarfs with hydrogen atmospheres. *Astrophys. J.* **543**, 216–226. https://doi.org/10.1086/317092 (2000).
20. Saumon, D., Hubbard, W. B., Chabrier, G. & van Horn, H. M. The role of the molecular-metallic transition of hydrogen in the evolution of Jupiter, Saturn, and brown dwarfs. *Astrophys. J* **391**, 827–831 (1992).
21. Daligault, J. & Gupta, S. Electron-ion scattering in dense multi-component plasmas: Application to the outer crust of an accreting star. *Astrophys. J.* **703**, 994–1011. https://doi.org/10.1088/0004-637x/703/1/994 (2009).
22. Moldabekov, Z. A. *et al.* Structural characteristics of strongly coupled ions in a dense quantum plasma. *Phys. Rev. E* **98**, 023207. https://doi.org/10.1103/PhysRevE.98.023207 (2018).
23. Bonitz, M. *et al.* Ab initio simulation of warm dense matter. *Phys. Plasmas* **27**, 042710. https://doi.org/10.1063/1.5143225 (2020).
24. Moses, E. I., Boyd, R. N., Remington, B. A., Keane, C. J. & Al-Ayat, R. The National Ignition Facility: Ushering in a new age for high energy density science. *Phys. Plasmas* **16**, 041006. https://doi.org/10.1063/1.3116505 (2009).
25. Fletcher, L. B. *et al.* Ultrabright X-ray laser scattering for dynamic warm dense matter physics. *Nat. Photonics* **9**, 274–279 (2015).
26. Bostedt, C. *et al.* Linac coherent light source: The first five years. *Rev. Mod. Phys.* **88**, 015007. https://doi.org/10.1103/RevModPhys.88.015007 (2016).
27. Glenzer, S. H. *et al.* Matter under extreme conditions experiments at the Linac Coherent Light Source. *J. Phys. B* **49**, 092001. https://doi.org/10.1088/0953-4075/49/9/092001 (2016).
28. Tschentscher, T. *et al.* Photon beam transport and scientific instruments at the European XFEL. *Appl. Sci.* **7**, 592. https://doi.org/10.3390/app7060592 (2017).
29. MacDonald, M. J. *et al.* Demonstration of a laser-driven, narrow spectral bandwidth X-ray source for collective X-ray scattering experiments. *Phys. Plasmas* **28**, 032708. https://doi.org/10.1063/5.0030958 (2021).
30. Vinko, S. M. *et al.* Creation and diagnosis of a solid-density plasma with an X-ray free-electron laser. *Nature* **482**, 59–62. https://doi.org/10.1038/nature10746 (2012).
31. Hansen, S. B. *et al.* Temperature determination using $k\alpha$ spectra from m-shell Ti ions. *Phys. Rev. E* **72**, 036408. https://doi.org/10.1103/PhysRevE.72.036408 (2005).
32. Ciricosta, O. *et al.* Direct measurements of the ionization potential depression in a dense plasma. *Phys. Rev. Lett.* **109**, 065002. https://doi.org/10.1103/PhysRevLett.109.065002 (2012).
33. Glenzer, S. H. *et al.* Demonstration of spectrally resolved X-ray scattering in dense plasmas. *Phys. Rev. Lett.* **90**, 175002. https://doi.org/10.1103/PhysRevLett.90.175002 (2003).
34. Humphries, O. S. *et al.* Probing the electronic structure of warm dense nickel via resonant inelastic X-ray scattering. *Phys. Rev. Lett.* **125**, 195001. https://doi.org/10.1103/PhysRevLett.125.195001 (2020).
35. Chen, Z. *et al.* Ultrafast multi-cycle terahertz measurements of the electrical conductivity in strongly excited solids. *Nat. Commun.* **12**, 1638. https://doi.org/10.1038/s41467-021-21756-6 (2021).
36. Glenzer, S. H. & Redmer, R. X-ray Thomson scattering in high energy density plasmas. *Rev. Mod. Phys* **81**, 1625 (2009).
37. Kraus, D. *et al.* Characterizing the ionization potential depression in dense carbon plasmas with high-precision spectrally resolved X-ray scattering. *Plasma Phys. Control Fusion* **61**, 014015 (2019).
38. Sólyom, J. *Fundamentals of the Physics of Solids* (Springer, 2010).
39. Döppner, T. *et al.* Temperature measurement through detailed balance in X-ray Thomson scattering. *High Energy Density Phys.* **5**, 182–186. https://doi.org/10.1016/j.hedp.2009.05.012 (2009).
40. Lindhard, J. On the properties of a gas of charged particles. *Matematisk-Fysiske Meddelelser Kongelige Danske Videnskabernes Selskab* **28**, 1–57 (1954).
41. Ichimaru, S. Strongly coupled plasmas: High-density classical plasmas and degenerate electron liquids. *Rev. Mod. Phys.* **54**, 1017–1059. https://doi.org/10.1103/RevModPhys.54.1017 (1982).
42. Ceperley, D. M. & Alder, B. J. Ground state of the electron gas by a stochastic method. *Phys. Rev. Lett.* **45**, 566–569. https://doi.org/10.1103/PhysRevLett.45.566 (1980).
43. Moroni, S., Ceperley, D. M. & Senatore, G. Static response and local field factor of the electron gas. *Phys. Rev. Lett.* **75**, 689–692. https://doi.org/10.1103/PhysRevLett.75.689 (1995).
44. Brown, E. W., Clark, B. K., DuBois, J. L. & Ceperley, D. M. Path-integral Monte Carlo simulation of the warm dense homogeneous electron gas. *Phys. Rev. Lett.* **110**, 146405. https://doi.org/10.1103/PhysRevLett.110.146405 (2013).
45. Dornheim, T. *et al.* Ab initio quantum Monte Carlo simulation of the warm dense electron gas in the thermodynamic limit. *Phys. Rev. Lett.* **117**, 156403. https://doi.org/10.1103/PhysRevLett.117.156403 (2016).
46. Dornheim, T. *et al.* Effective static approximation: A fast and reliable tool for warm-dense matter theory. *Phys. Rev. Lett.* **125**, 235001. https://doi.org/10.1103/PhysRevLett.125.235001 (2020).
47. Dornheim, T., Moldabekov, Z. A. & Tolias, P. Analytical representation of the local field correction of the uniform electron gas within the effective static approximation. *Phys. Rev. B* **103**, 165102. https://doi.org/10.1103/PhysRevB.103.165102 (2021).
48. Mermin, N. D. Lindhard dielectric function in the relaxation-time approximation. *Phys. Rev. B* **1**, 2362 (1970).
49. Reinholz, H., Redmer, R., Röpke, G. & Wierling, A. Long-wavelength limit of the dynamical local-field factor and dynamical conductivity of a two-component plasma. *Phys. Rev. E* **62**, 5648–5666. https://doi.org/10.1103/PhysRevE.62.5648 (2000).
50. Fortmann, C., Wierling, A. & Röpke, G. Influence of local-field corrections on Thomson scattering in collision-dominated two-component plasmas. *Phys. Rev. E* **81**, 026405. https://doi.org/10.1103/PhysRevE.81.026405 (2010).
51. Hohenberg, P. & Kohn, W. Inhomogeneous electron gas. *Phys. Rev.* **136**, B864–B871. https://doi.org/10.1103/PhysRev.136.B864 (1964).
52. Kohn, W. & Sham, L. J. Self-consistent equations including exchange and correlation effects. *Phys. Rev.* **140**, A1133–A1138. https://doi.org/10.1103/PhysRev.140.A1133 (1965).
53. Runge, E. & Gross, E. K. U. Density-functional theory for time-dependent systems. *Phys. Rev. Lett.* **52**, 997–1000. https://doi.org/10.1103/PhysRevLett.52.997 (1984).
54. Pribram-Jones, A., Gross, D. A. & Burke, K. DFT: A theory full of holes?. *Ann. Rev. Phys. Chem.* **66**, 283–304. https://doi.org/10.1146/annurev-physchem-040214-121420 (2015).
55. Lejaeghere, K. *et al.* Reproducibility in density functional theory calculations of solids. *Science* **351**, 1415-U81. https://doi.org/10.1126/science.aad3000 (2016).
56. Kietzmann, A., Redmer, R., Desjarlais, M. P. & Mattsson, T. R. Complex behavior of fluid lithium under extreme conditions. *Phys. Rev. Lett.* **101**, 070401. https://doi.org/10.1103/PhysRevLett.101.070401 (2008).
57. Baczewski, A. D., Shulenburger, L., Desjarlais, M. P., Hansen, S. B. & Magyar, R. J. X-ray Thomson scattering in warm dense matter without the Chihara decomposition. *Phys. Rev. Lett.* **116**, 115004. https://doi.org/10.1103/PhysRevLett.116.115004 (2016).
58. Ramakrishna, K., Cangi, A., Dornheim, T., Baczewski, A. & Vorberger, J. First-principles modeling of plasmons in aluminum under ambient and extreme conditions. *Phys. Rev. B* **103**, 125118. https://doi.org/10.1103/PhysRevB.103.125118 (2021).
59. Sperling, P. *et al.* Free-electron X-ray laser measurements of collisional-damped plasmons in isochorically heated warm dense matter. *Phys. Rev. Lett.* **115**, 115001. https://doi.org/10.1103/PhysRevLett.115.115001 (2015).

60. Witte, B. B. L. *et al.* Warm dense matter demonstrating non-drude conductivity from observations of nonlinear plasmon damping. *Phys. Rev. Lett.* **118**, 225001. https://doi.org/10.1103/PhysRevLett.118.225001 (2017).

61. Mo, C., Fu, Z., Kang, W., Zhang, P. & He, X. T. First-principles estimation of electronic temperature from X-Ray Thomson scattering spectrum of isochorically heated warm dense matter. *Phys. Rev. Lett.* **120**, 205002. https://doi.org/10.1103/PhysRevLett.120.205002 (2018).

62. Ma, T. *et al.* X-ray scattering measurements of strong ion–ion correlations in shock-compressed aluminum. *Phys. Rev. Lett.* **110**, 065001. https://doi.org/10.1103/PhysRevLett.110.065001 (2013).

63. Sawada, H. *et al.* 2D monochromatic X-ray imaging for beam monitoring of an X-ray free electron laser and a high-power femtosecond laser. *Rev. Sci. Instrum.* **92**, 013510. https://doi.org/10.1063/5.0014329 (2021).

64. Šmíd, *et al.* Mirror to measure small angle X-ray scattering signal in high energy density experiments. *Rev. Sci. Instrum.* **91**, 123501. https://doi.org/10.1063/5.0021691 (2020).

65. Kluge, T. *et al.* Observation of ultrafast solid-density plasma dynamics using femtosecond X-ray pulses from a free-electron laser. *Phys. Rev. X* **8**, 031068. https://doi.org/10.1103/PhysRevX.8.031068 (2018).

66. Ofori-Okai, B. K. *et al.* A terahertz pump mega-electron-volt ultrafast electron diffraction probe apparatus at the SLAC accelerator structure test area facility. *J. Instrum.* **13**, P06014–P06014 (2018).

67. Zastrau, U. *et al.* Resolving ultrafast heating of dense cryogenic hydrogen. *Phys. Rev. Lett* **112**, 105002 (2014).

68. Clrouin, J. *et al.* Self-organization in dense plasmas: The gamma-plateau. *Contrib. Plasma Phys.* **55**, 159–163. https://doi.org/10.1002/ctpp.201400064 (2015).

69. Grabowski, P. *et al.* Review of the first charged-particle transport coefficient comparison workshop. *High Energy Density Phys.* **37**, 100905. https://doi.org/10.1016/j.hedp.2020.100905 (2020).

70. Moroni, S., Ceperley, D. M. & Senatore, G. Static response from quantum Monte Carlo calculations. *Phys. Rev. Lett.* **69**, 1837–1840. https://doi.org/10.1103/PhysRevLett.69.1837 (1992).

71. Dornheim, T., Groth, S. & Bonitz, M. The uniform electron gas at warm dense matter conditions. *Phys. Rep.* **744**, 1–86. https://doi.org/10.1016/j.physrep.2018.04.001 (2018).

72. Dornheim, T., Vorberger, J. & Bonitz, M. Nonlinear electronic density response in warm dense matter. *Phys. Rev. Lett.* **125**, 085001. https://doi.org/10.1103/PhysRevLett.125.085001 (2020).

73. Yan, J., Mortensen, J. J., Jacobsen, K. W. & Thygesen, K. S. Linear density response function in the projector augmented wave method: Applications to solids, surfaces, and interfaces. *Phys. Rev. B* **83**, 245122. https://doi.org/10.1103/PhysRevB.83.245122 (2011).

74. Dandrea, R. G., Ashcroft, N. W. & Carlsson, A. E. Electron liquid at any degeneracy. *Phys. Rev. B* **34**, 2097–2111. https://doi.org/10.1103/PhysRevB.34.2097 (1986).

75. Egerton, R. F. Electron energy-loss spectroscopy in the TEM. *Rep. Prog. Phys.* **72**, 016502. https://doi.org/10.1088/0034-4885/72/1/016502 (2008).

76. Giuliani, G. & Vignale, G. *Quantum Theory of the Electron Liquid* (Cambridge University Press, 2008).

77. Mortensen, J. J., Hansen, L. B. & Jacobsen, K. W. Real-space grid implementation of the projector augmented wave method. *Phys. Rev. B* **71**, 035109. https://doi.org/10.1103/PhysRevB.71.035109 (2005).

78. Enkovaara, J. *et al.* Electronic structure calculations with GPAW: A real-space implementation of the projector augmented-wave method. *J. Phys.: Condens. Matter* **22**, 253202. https://doi.org/10.1088/0953-8984/22/25/253202 (2010).

79. Larsen, A. H. *et al.* The atomic simulation environment—A python library for working with atoms. *J. Phys.: Condens. Matter* **29**, 273002 (2017).

80. Bahn, S. R. & Jacobsen, K. W. An object-oriented scripting interface to a legacy electronic structure code. *Comput. Sci. Eng.* **4**, 56–66. https://doi.org/10.1109/5992.998641 (2002).

81. Perdew, J. P. & Zunger, A. Self-interaction correction to density-functional approximations for many-electron systems. *Phys. Rev. B* **23**, 5048–5079. https://doi.org/10.1103/PhysRevB.23.5048 (1981).

82. See Supplemental Material for additional details.

83. Hamann, P., Vorberger, J., Dornheim, T., Moldabekov, Z. A. & Bonitz, M. Ab initio results for the plasmon dispersion and damping of the warm dense electron gas. *Contrib. Plasma Phys.* **60**, e202000147. https://doi.org/10.1002/ctpp.202000147 (2020).

84. Preston, T. R. *et al.* Measurements of the momentum-dependence of plasmonic excitations in matter around 1 Mbar using an X-ray free electron laser. *Appl. Phys. Lett.* **114**, 014101. https://doi.org/10.1063/1.5070140 (2019).

85. Descamps, A. *et al.* An approach for the measurement of the bulk temperature of single crystal diamond using an X-ray free electron laser. *Sci. Rep.* **10**, 14564. https://doi.org/10.1038/s41598-020-71350-x (2020).

86. Zastrau, U. *et al.* Resolving ultrafast heating of dense cryogenic hydrogen. *Phys. Rev. Lett.* **112**, 105002. https://doi.org/10.1103/PhysRevLett.112.105002 (2014).

87. Kulcsár, G. *et al.* Intense picosecond X-ray pulses from laser plasmas by use of nanostructured "velvet" targets. *Phys. Rev. Lett.* **84**, 5149–5152. https://doi.org/10.1103/PhysRevLett.84.5149 (2000).

88. Dornheim, T., Groth, S. & Bonitz, M. The uniform electron gas at warm dense matter conditions. *Phys. Rep.* **744**, 1–86 (2018).

89. Ceperley, D. M. Path integrals in the theory of condensed helium. *Rev. Mod. Phys* **67**, 279 (1995).

90. Dornheim, T. Fermion sign problem in path integral Monte Carlo simulations: Quantum dots, ultracold atoms, and warm dense matter. *Phys. Rev. E* **100**, 023307 (2019).

Acknowledgements

Author contributions

Z.A.M. performed the DFT simulations, analyzed the results, and greatly contributed to composing the manuscript. T.D. performed QMC simulations and contributed to the manuscript. A.C. analyzed the results and greatly contributed to composing the manuscript.

Funding

Competing interests

The authors declare no competing interests.

Additional information

Supplementary Information The online version contains supplementary material available at https://doi.org/10.1038/s41598-022-05034-z.

Correspondence and requests for materials should be addressed to A.C.

Reprints and permissions information is available at www.nature.com/reprints.

Publisher's note Springer Nature remains neutral with regard to jurisdictional claims in published maps and institutional affiliations.